Raman spectroscopy of hydrogenated amorphous carbons

C. Casiraghi, A. C. Ferrari,* and J. Robertson
Department of Engineering, University of Cambridge, Cambridge CB2 1PZ, United Kingdom
(Received 10 March 2005; revised manuscript received 16 May 2005; published 1 August 2005)

We present a comprehensive multiwavelength Raman investigation of a variety of hydrogenated amorphous carbons (*a*-C:H), ranging from polymeric *a*-C:H to diamond-like *a*-C:H and ta-C:H, which allows us to derive values for their bonding, density, band gap, hydrogen content, and mechanical properties. The Raman spectra of *a*-C:Hs show two different trends. In one case, the *G* peak width increases with *G* peak dispersion. In the second case, the opposite trend is found. In the first case, the Raman parameters vary with optical, structural, and mechanical properties in the same way as in hydrogen-free carbon films. In the second case, typical of polymeric *a*-C:H, the *G* peak width correlates with the density, while the *G* peak dispersion varies with the optical gap and hydrogen content. This allows a unified picture of bonding and disorder of all carbon films. UV Raman is particularly useful for *a*-C:Hs, as it gives clear measurements in the *D* and *G* peaks spectral region even for highly hydrogenated samples, for which the visible Raman spectra are overshadowed by photoluminescence. On the other hand, the slope of the photoluminescence background in visible Raman spectra can be used to estimate the H content. UV Raman measurements also allow the detection of C—H stretching vibrations.

DOI: 10.1103/PhysRevB.72.085401 PACS number(s): 78.30.Ly, 63.50.+x, 61.43.Dq

I. INTRODUCTION

Diamond-like carbon (DLC) is an amorphous carbon with a significant fraction of CC sp^3 bonds.[1,2] Tetrahedral amorphous carbon (ta-C) is the DLC with the maximum sp^3 content. We classify hydrogenated amorphous carbons into four types, as shown in Fig. 1.[3]

(1) *a*-C:H films with the highest H content (40–60 at. %). These films can have up to 70% sp^3.[1] However, most of the sp^3 bonds are hydrogen terminated and this material is soft and has low density.[1] We call these films polymer-like *a*-C:H (PLCH). Their band gap ranges from 2 eV to 4 eV.[1] These films are usually deposited by plasma enhanced chemical vapor deposition (PECVD) at low bias voltage.[1,2,4]

(2) *a*-C:H films with intermediate H content (20–40 at. %). Even if these films have lower overall sp^3 content, they have more C—C sp^3 bonds than PLCH. Thus, they have better mechanical properties.[1] Their optical gap is between 1 and 2 eV.[1] We call these films diamond-like *a*-C:H (DLCH). They are usually deposited by PECVD[1,2,4] or electron cyclotron resonance (ECR) or reactive sputtering at moderate bias voltage.[5–7]

(3) Hydrogenated tetrahedral amorphous carbon films (ta-C:H). ta-C:H films are a class of DLCH in which the CC sp^3 content can be increased while keeping a fixed H content, as in Fig. 1. Many films defined in literature as ta-C:H are just DLCHs. However, due to the highest sp^3 content (~70%) and 25–30 at. % H, ta-C:Hs are really a different category as indicated by their Raman spectra, their higher density (up to 2.4 g/cm^3) and Young's modulus (up to 300 GPa).[8] Their optical gap can reach 2.4 eV.[9] These films are deposited by high-density plasma sources such as electron cyclotron wave resonance (ECWR)[9,10] and plasma beam source (PBS).[11,12] An alternative way to produce ta-C:H was also attempted by introducing H while depositing ta-C by filtered cathodic vacuum arc (FCVA).[13]

(4) *a*-C:H with low H content (less than 20 at. %). They have a high sp^2 content. The gap is under 1 eV. We call these films graphite-like *a*-C:H (GLCH). They are usually deposited by PECVD at high bias,[1,2,4] dc glow discharge (GD) systems,[14] or magnetron sputtering (MS).[15]

Raman spectroscopy is a fast and nondestructive method for the characterization of carbon materials.[16] All carbons show common features in their Raman spectra in the 800–2000 cm^{-1} region, the so-called *G* and *D* peaks, which lie at around 1560 and 1360 cm^{-1}, respectively, for visible excitation, and the *T* peak at around 1060 cm^{-1}, which is only seen for UV excitation.[17–21] The *G* peak is due to the bond stretching of all pairs of sp^2 atoms in both rings and chains. The *D* peak is due to the breathing modes of sp^2 atoms in rings.[17,22–25] The *T* peak is due to the C—C sp^3 vibrations.[19–21]

In previous papers we have shown that multiwavelength Raman spectra can be used to distinguish the different types of amorphous carbons and to derive their structural and mechanical properties. We discussed hydrogen-free amorphous

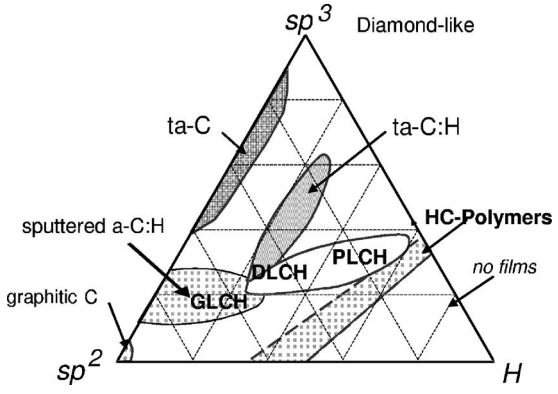

FIG. 1. Ternary phase diagram for H free and hydrogenated amorphous carbons.

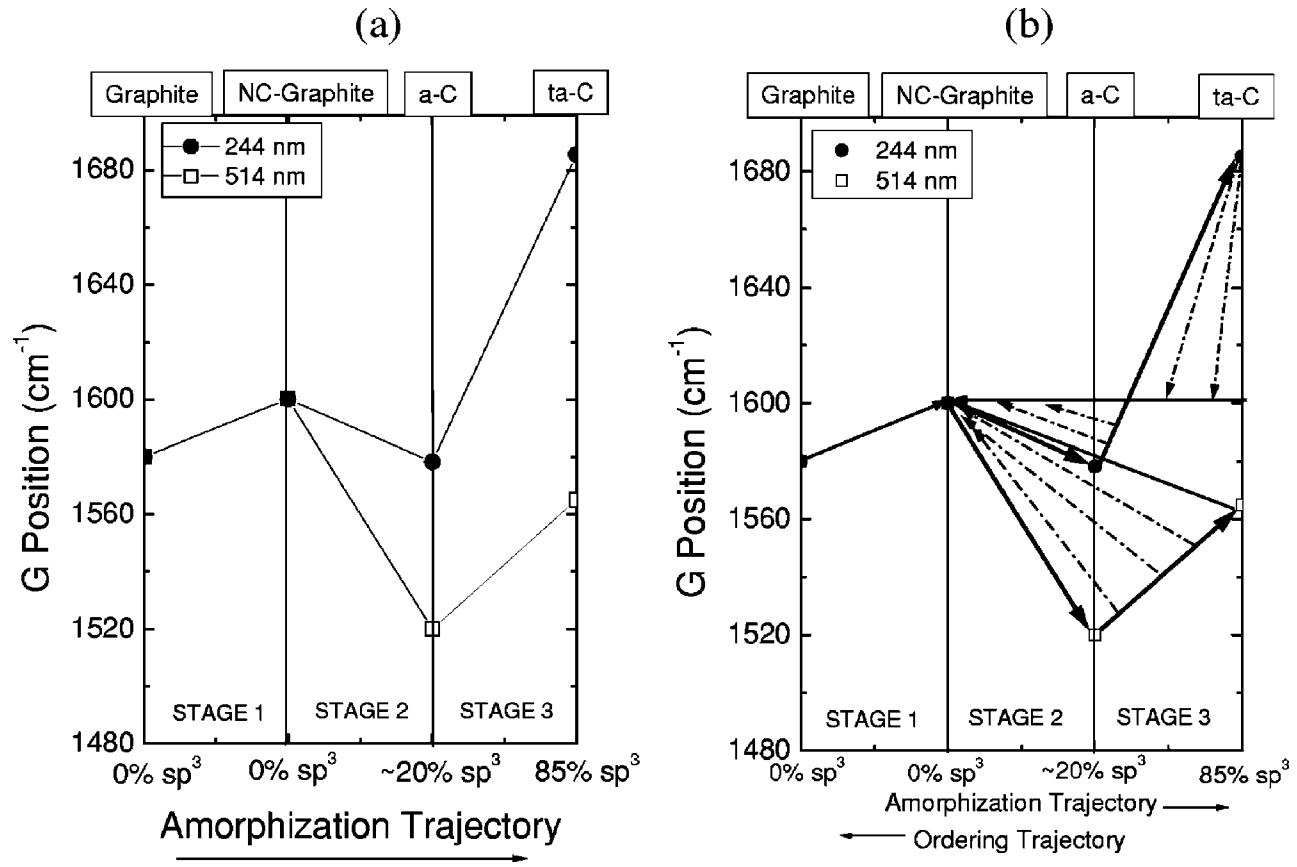

FIG. 2. (a) Amorphization trajectory, showing the schematic variation of the G position for 244 and 514.5 nm excitation energies. (b) Amorphization trajectory, showing the possibility of non-uniqueness in stages 2 and 3 for 244 and 514.5 nm excitation energies wavelengths (Ref. 18).

carbons,[17,18] amorphous carbon nitrides,[26] and nanodiamond.[27] In this paper, we present a detailed study of the Raman spectra of hydrogenated amorphous carbons. We apply and extend our previous three-stage model and we derive a unified picture of bonding and disorder in carbons, from two Raman parameters: the G peak width and the G peak dispersion.

This paper is organized as follows. In Sec. II we discuss the background concepts for this paper. In Sec. III we give the experimental details on the samples, the characterization techniques used to derive the relevant properties, and the Raman measurements and fitting procedures. In Sec. IV we present our main experimental observations and, in particular, a set of useful correlations between single and multiwavelength Raman parameters and structure of the films. In Sec. V we extend the three-stage model to include hydrogenated amorphous carbons.

II. BACKGROUND

We desire to use Raman spectroscopy to extract bonding parameters of DLCs, such as density, sp^3 fraction, or H content. However, Raman spectroscopy is mainly sensitive to the configuration of sp^2 sites because of their higher cross section. The way to derive these properties is a model that relates sp^2 site disorder to the overall bonding, the so-called three-stage model.[17,18]

The three-stage model[17,18] describes the evolution of the Raman spectra of carbons in terms of an amorphization trajectory, starting from perfect graphite, Figs. 2(a) and 2(b). The Raman spectra are dominated by the sp^2 sites. Thus, the clustering and disorder of the sp^2 phase is the main factor affecting peak positions, width, and intensity. In principle, the sp^2 clustering can vary independently of the sp^3 content. This means one visible Raman spectrum could correspond to films with different sp^3 content. Combining a visible Raman spectrum with a UV Raman spectrum helps in resolving this problem. For UV Raman excitation the G peak position decreases with increasing sp^2 clustering. If two samples have similar G peak positions in visible Raman but different ones in UV Raman, the sample with the lower G position in UV has higher sp^2 clustering, Fig. 2(b). Thus, a multiwavelength Raman analysis is able to fully characterize DLCs. The combination of visible and UV Raman spectra can be used to define the G peak dispersion, Disp(G), i.e., the rate of change of G peak position with excitation wavelength.

The other two key Raman parameters to monitor carbon bonding are the intensity ratio of the D and G peaks, $I(D)/I(G)$, and the full width at half maximum of the G peak, FWHM(G). In amorphous carbons $I(D)/I(G)$ is a measure of the size of the sp^2 phase organized in rings.[17] If $I(D)/I(G)$ is negligible, then the sp^2 phase is mainly organized in chains, or, even if rings are present, the π bonds are not fully delocalized on the rings.[17]

FWHM(G) and Disp(G) both measure disorder, *however, FWHM(G) is mainly sensitive to structural disorder, while Disp(G) is mainly sensitive to topological disorder*. Structural disorder arises from bond angle and bond length distortions. Topological disorder arises from the size and shape distribution of sp^2 clusters.

Samples with a sp^2 phase entirely constituted of fully π delocalized rings do not show any G peak dispersion.[18] The G peak dispersion arises from the resonant selection of sp^2 chains of different sizes at different excitation energies.[18,19] By the size of the sp^2 chain we mean the effective chain conjugation length. In this framework, a long, strained sp^2 chain, with defects interrupting the π delocalization, is equivalent to a set of smaller chains. Thus, the G peak dispersion is mainly a measure of topological disorder. In contrast, the G peak width is a single wavelength parameter. It probes those sp^2 clusters resonant at a particular excitation energy. Clusters probed at a given excitation energy have roughly similar size. FWHM(G) would be small if the clusters were defect-free, unstrained or "molecular." For a given cluster size, a higher bond length and bond angle disorder lead to a higher FWHM(G). This implies that FWHM(G) is mainly a probe of structural disorder. Higher excitation energies are resonant with smaller clusters. This allows smaller differences between configurations and so FWHM(G) decreases with excitation energy.[18,26,28]

In hydrogen-free carbons, the structural and topological disorder vary in parallel along the amorphization trajectory.[18] FWHM(G) and Disp(G) both increase as disorder increases, for all excitation energies.[18,26] The increase of disorder is linked to higher sp^3 content, density, and mechanical properties, which causes the correlation between multi-wavelength Raman spectra and mechanical properties seen previously.[18,28,29]

This still holds for a-C:H's with H contents under 20–30 at. %, such as ta-C:H, DLCH, and GLCH. By further increasing the amount of hydrogen over 25% at., the overall sp^3 content can still increase, but not the C—C sp^3 content. Indeed, PLCHs have the smallest defect density of any carbon films, together with the smallest mass density and stress. Structural disorder now decreases with H content, while topological disorder continues to increase,[30] so that FWHM(G) and Disp(G) will have opposite trends.

Hydrogen has a further important effect, which helps the analysis of the Raman spectra. Contrary to the introduction of nitrogen[26] or to the effect of annealing,[18,31] the introduction of hydrogen into an amorphous carbon links the amount and configuration of the sp^2 phase with the overall sp^3 content (C—C+C—H sp^3). In principle, this is quite fortunate, as it implies that for a-C:H a single wavelength Raman study could be enough to quantify the H and sp^3 content, the optical, and mechanical properties. However, we urge extreme caution when doing a single wavelength analysis, since there are some deposition processes that can introduce sp^2 rings even in samples with high H content. In these cases, multi-wavelength Raman spectroscopy is necessary to extract reliable information.

Due to the overwhelming cross section of sp^2 sites for visible excitation, the C—H stretching modes can only be seen for UV excitation.[18] However, a typical signature of hydrogenated samples in visible Raman spectra is the increasing photoluminescence (PL) background for higher H content. This is due to the hydrogen saturation of nonradiative recombination centers.[32–34] The ratio between the slope m of the fitted linear background and the intensity of the G peak, $m/I(G)$, can be empirically used as a measure of the bonded H content, as will be shown in Sec. IV.

For H contents over 40–45 at. %, the PL background obscures the Raman signal for visible excitation[7,35–38] but not for UV excitation. This means that we will mainly refer to the FWHM(G) for UV excitation in the following sections because it can be measured for every film.

III. EXPERIMENT

We studied more than 60 a-C:H samples prepared with different deposition systems: (1) 13.56 MHz rf PECVD system, with pressure and rf power ranging from 0.02 to $\sim$20 mbar and 10–250 W, respectively; (2) ECWR source.[9,39] The rf power was 600 W and the plasma pressure was ranging from 1 to 6×10^{-3} mbar.[39] For these deposition systems we considered two gases, CH_4 and C_2H_2; (3) Distributed electron cyclotron resonance (DECR) plasma reactor.[40–42] In this case only C_2H_2 was used as precursor; (4) Magnetron sputtering in an Ar/H_2 atmosphere from a graphite target with flow ratios in the range 0.025–0.9, and pressures from 2.5×10^{-5} to 1×10^{-3};[15,43] and (5) FCVA, used with a H_2 supply to produce hydrogenated samples, as described in Ref. 13. Further data were derived from literature.[4,6,7,43–50]

For comparison, we also considered the Raman spectra of some H free carbons: nanocrystalline graphite (nc-G), an amorphous carbon deposited by MS, and a ta-C deposited by FCVA, as described in Refs. 17, 18, and 28.

All the samples produced in our laboratory were deposited simultaneously on silicon (for Raman measurements) and on quartz (for optical gap measurements). The substrates were cleaned in ultrasonic bath.

The density and hydrogen content ($\pm5\%$) of the samples were determined from nuclear reaction analysis (NRA). The optical gap (Tauc gap, E_T, and E_{04}) was derived by UV-visible spectrophotometry. The Young's modulus (E) was measured by the laser acoustic wave technique or by surface Brillouin scattering.[51,52]

Unpolarized Raman spectra were measured at 244 and 514 nm excitations using Renishaw micro-Raman 1000 spectrometers. The UV Raman spectra are collected with a 40× objective and a UV-enhanced charge-coupled device camera. The spectral resolution is ~6 cm^{-1}. All the UV Raman spectra are corrected by subtracting the background signal due to the optics. This is done by measuring an Al mirror background signal and normalizing this signal so that the atmospheric N_2 peak at ~2332 cm^{-1}, detected for the mirror measurement, has the same intensity of the corresponding atmospheric N_2 peak, detected on the sample. Contrary to ta-C, hydrogenated amorphous carbons are particularly sensitive to UV excitation and can be easily damaged. In order to avoid damage, the power on the sample is kept well below

1 mW (down to 0.005 mW) and the samples are placed on a spinner rotating at high speed (>3000 rpm). The acquisition time is in the 5–60 s range, adjusted to minimize the noise but still kept below the damage threshold. The change in acquisition time is allowed here, since what matters is the overall shape of the spectra, not their absolute intensity. These accurate procedures ensure no visible damage is produced on the sample surface and no change of the spectral shape during the measurements. The visible Raman spectra are collected with a 100× objective. The spectral resolution is ~2 cm^{-1}. The power on the samples is always kept below 4 mW (down to 0.4 mW) and the acquisition time is always less than 90 s in order to avoid damage.

There are two main options for spectral shape fitting: an all Gaussians fit or a fit with a Breit-Wigner-Fano (BWF) line shape for the *G* peak and a Lorentzian for the *D* peak. For samples with a significant PL background, such as the ones studied here, the BWF line is not the most appropriate since the coupling coefficient is influenced by the PL slope and thus the BWF tends to adjust its asymmetry to reproduce part of the PL slope. This does not allow reproducible fits of the PL background. On the other hand, fully symmetric Gaussian lines work better in the presence of a background. They also allow a direct comparison with previous studies using Gaussian fitting.[7,45,49] In any case, the crucial point, once the fitting procedure is decided, is to consistently use it for the whole set of samples one wishes to study. A different, but properly converged and stable fitting procedure, will yield the same trends, even if the absolute numbers can be slightly different.

Room temperature micro-photoluminescence was measured for 514 nm excitation using a Renishaw RM-1000 spectrometer fitted with a low dispersion grating (600 groves/mm). The spectra were recorded in the 520–850 nm spectral range (2.4–1.46 eV). The main PL peak is fitted with one Gaussian. The PL intensity is normalized to the Raman *G* peak intensity. On the other hand, the PL background is measured from the 514 nm Raman spectra. This is defined as the ratio between the slope of the Raman spectra (m) between 1050 and 1800 cm^{-1}, and the intensity of the *G* peak, $m/I(G)$.

We also study the spectral region 2800–3400 cm^{-1} of the UV Raman spectra. This contains information on the sp^3 CH_x ($x=2,3$) and sp^2 aromatic and olefinic stretching vibrations.[53] Since the frequencies of these modes are very close and the spectra are broad, it is not possible to make a precise quantitative mode analysis as previously done in infrared spectroscopy (IR).[54,55] However, by UV Raman spectroscopy one can assess films deposited on substrates unsuitable for IR measurements.

The following fit parameters are thus considered in this study: Pos(*G*), Disp(*G*), FWHM(*G*), $m/I(G)$, $I(D)/I(G)$, and the area ratio of the *D* and *G* peaks, $A(D)/A(G)$. In this paper the area ratio is used only for convenience, since it allows us to perform a direct comparison with some previously published data, reported only as the area ratio.[7,45,49] However, it must be noted that the area ratio is not the best parameter to use, since it is equivalent to the product of the intensity and width ratios, which are better studied separately, since they contain different information.

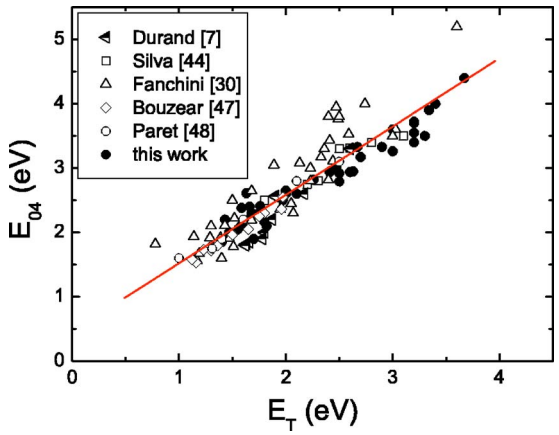

FIG. 3. (Color online) E_{04} as a function of Tauc gap. The linear fit is shown.

When our comments on the trends of the Raman parameters are meant to be general, we will not specify the excitation wavelength. When we refer to particular excitations, we will indicate this by adding @wavelength to the parameter. For example, FWHM(*G*)@244 indicates the FWHM of the *G* peak measured at 244 nm.

IV. RESULTS

The experimental relation between E_{04} and E_T measured for our samples and from literature data[7,30,44,47,48] is shown in Fig. 3. By fitting the data in Fig. 3 we find

$$E_{04}\,(\mathrm{eV}) = 0.46 + 1.06E_T\,(\mathrm{eV}). \quad (1)$$

This was used to estimate E_T from some literature data, when only E_{04} was reported or vice versa.

Figures 4(a) and 4(b) show the 514 and 244 nm Raman spectra measured on films representative of the four *a*-C:H classes described in Sec. I. Note that for low H content, the visible spectra do not exhibit a PL background, while the PL is so strong for the highest H content that the visible spectrum is featureless. In contrast, a Raman spectrum can always be measured for UV excitation, irrespective of the H content. Indeed, UV Raman spectra with two well-separated features, such as the top spectra in Fig. 4(b), are an unambiguous signature of PLCH films.[18]

Figures 5(a) and 5(b) plot Pos(*G*)@514 and $I(D)/I(G)$@514 as a function of the H content. If H >20 at. %, Pos(*G*)@514 and $I(D)/I(G)$@514 decrease with increasing H content. At low H content, there is no obvious link between the Raman parameters and H content. This is simple to understand if one considers that different structures of amorphous carbons are possible for $H=0$, ranging from graphite to ta-C. In Fig. 5 and in the following figures a line indicates the extrapolation to low H content of the ideal trend for as-deposited hydrogenated samples. Similarly, the nonuniqueness regions are represented by shadowed areas.

Both optical gap and visible Raman spectra change according to the clustering of the sp^2 phase.[1,17,18] However, PLCH and ta-C samples, although having a similar gap, have

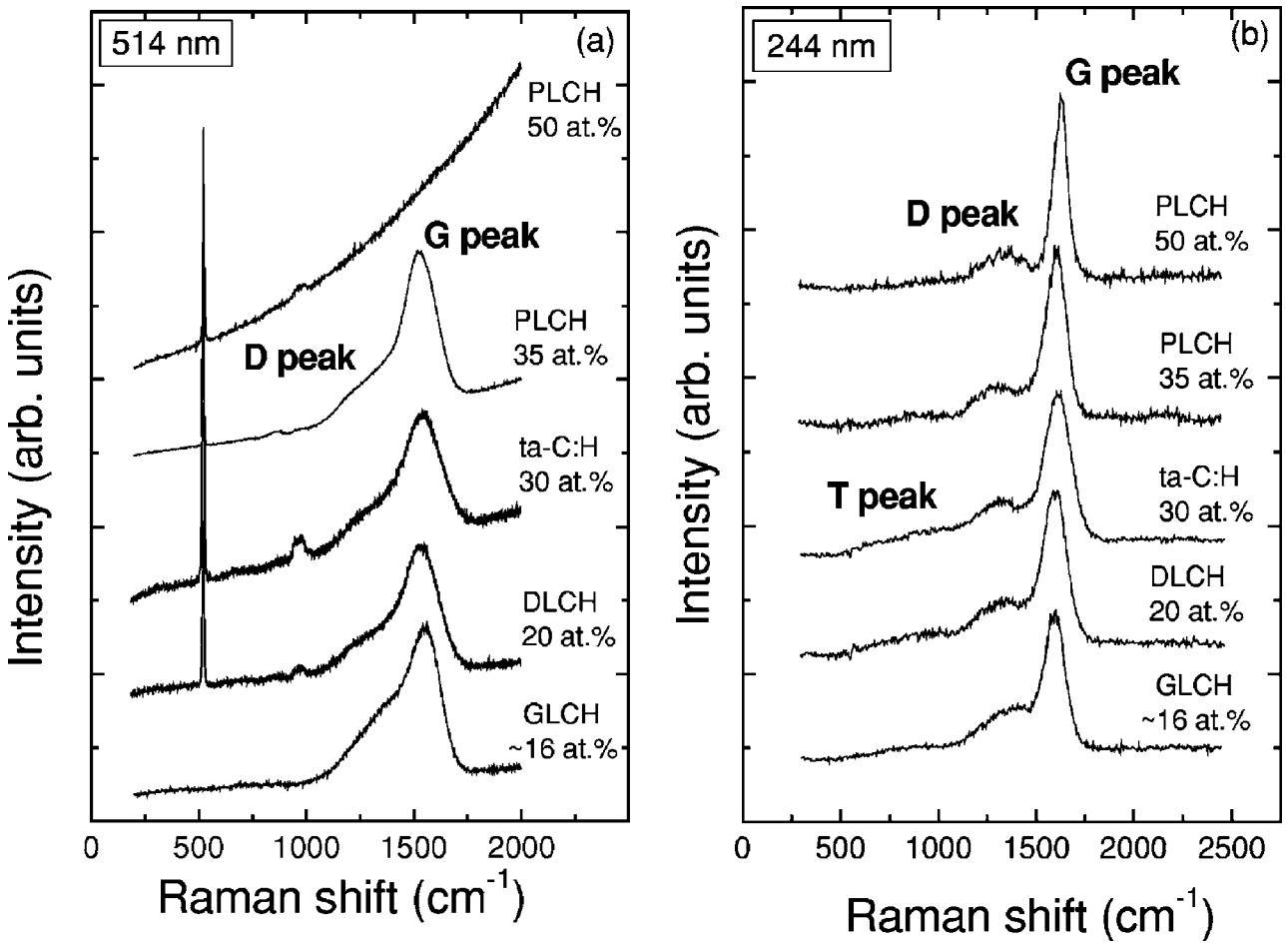

FIG. 4. Raman spectra of template a-C:H films at (a) 514.5 and (b) 244 nm.

a very different Pos(G)@514, as in Fig. 6. The same happens for low gap a-C and nanocrystralline graphite (nc-G). This results in the nonuniqueness region shown in Fig. 6. However, for H $>$ 20 at. % there is a unique relation between visible Raman spectra and optical gap. The same unique relation is observed between visible Raman spectra and H content (Fig. 5). Indeed, optical gap and H content are proportional for H $>$ 20 at. %, as shown in Fig. 7. By fitting the data in Fig. 7 (Refs. 7,45,48,50,56,57) we get a formula relating H content and Tauc gap for H $>$ 20 at. %

$$E_T\,[\mathrm{eV}] = -0.9 + 0.09 \cdot \mathrm{H}\,[\mathrm{at.\ \%}]. \qquad (2)$$

The 514 nm Raman spectra also provide information on the H content via the PL slope. Figure 8 plots the room temperature PL data for films with H contents of 20 to 35 at. % and some H-free amorphous carbons. The spectra have been normalized to the G peak intensity.

Note that some samples can have Tauc gaps over 2.41 eV, the laser excitation energy used for PL and Raman measurements. Thus, if the gap is over 2.41 eV, we only probe the PL of sub band-gap clusters. This nevertheless allows an estimate of the H content, because the recombination efficiency of sub band-gap clusters also increases with H content.[32–34] This is demonstrated in Fig. 9(a) where we plot the average PL peak position as a function of the optical gap for various films measured by us or taken from literature.[33,34,36,58,59] The PL peak position is seen to saturate when the optical gap exceeds the excitation energy. On the other hand, Fig. 9(b) shows that, by normalizing to the Raman intensity, the PL intensity continues to increase with H content, even for subgap excitation. Normalizing to the G peak intensity is reasonable since, if we neglect the possible variation of 514 nm Raman cross section across the different a-C:H samples, the Raman and PL intensities both have a similar dependence on sample thickness, absorption coefficient, and laser penetration depth. Thus, for practical purposes, it is not necessary to measure PL over a wide spectral range, as in Fig. 8, but we can take the PL background under the D and G peak spectral regions. Note that PL has sometimes been seen in some H-free carbons (Fig. 8 and Ref. 60). However, the PL intensity in H-free samples is at least four times lower than that of PLCH, see Fig. 9(b). Also note that, for low density and porous carbons such as in Ref. 60, the PL may be associated with adsorbed water during deposition in poor vacuum conditions or after exposure to air.[61,62]

Figure 10(a) shows that the normalized PL slope, $m/I(G)$, increases exponentially with the hydrogen content, for all films examined. The data of Fig. 10(a) give a simple quantitative formula for the hydrogen content

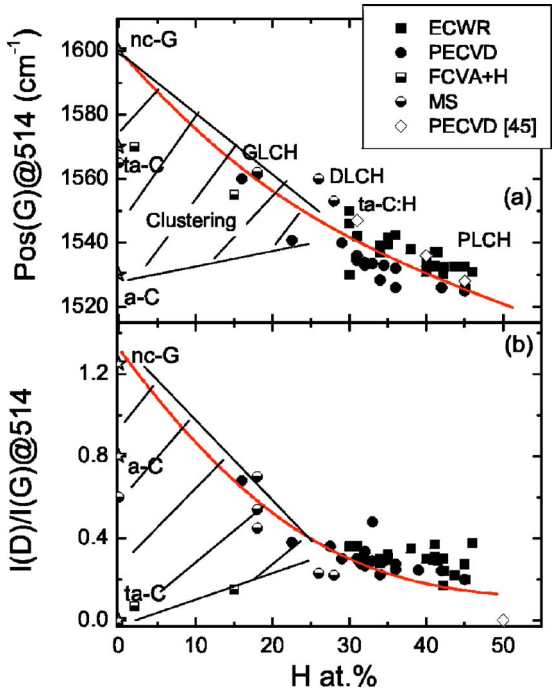

FIG. 5. (Color online) (a) Pos(G)@514.5 and (b) $I(D)/I(G)$@514.5 nm as a function of H content. The ideal trajectories of the Raman parameters with H incorporation from nc-G are marked by a line. The shaded regions represent the non-uniqueness at low H contents.

$$\mathrm{H}\,[\text{at. }\%] = 21.7 + 16.6 \log\left\{\frac{m}{I(G)}\,[\mu m]\right\}. \qquad (3)$$

Figure 10(b) shows that $m/I(G)$ also increases exponentially with the Tauc gap for H$>$20 at. %.

Figure 11 plots the spin density in DLCH and PLCH as a function of the gap (E_{04}) using data from literature.[11,44,48,63–68] It also plots the fitting line between $m/I(G)$ and E_{04} (bottom X axis) or H content (top X axis). Figure 11 clearly shows that there is a general relation between the decrease of spin density and an increase of PL efficiency, since both spin density and $m/I(G)$ have a similar trend as a function of E_{04} or H content in the range plotted in Fig. 11. For lower gap or H content the PL intensity is negligible.

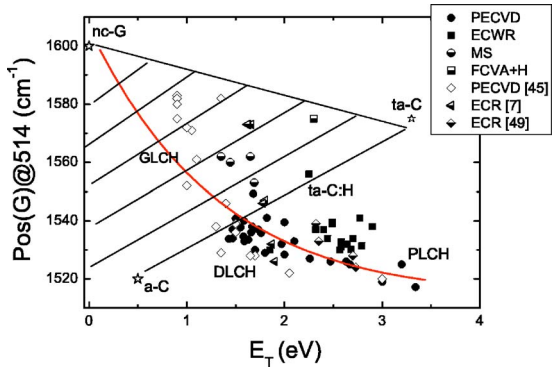

FIG. 6. (Color online) Pos(G)@514.5 as a function of Tauc gap. The ideal trajectory with H incorporation from nc-G is marked by a line. The shaded region represents the non-uniqueness at low H contents.

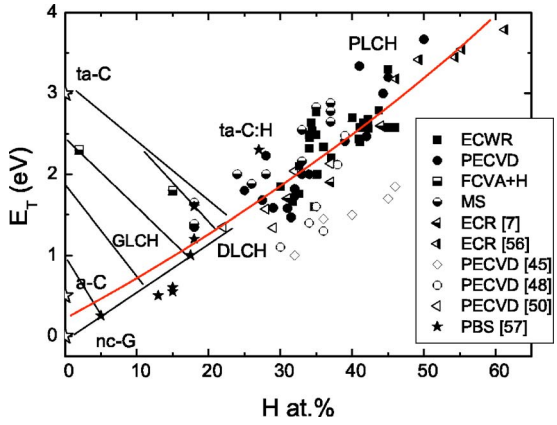

FIG. 7. (Color online) Tauc gap as a function of H content. The ideal trajectory with H incorporation from nc-G is marked by a line. The shaded region represents the non-uniqueness at low H contents.

Figures 12(a) and 12(b) plot Disp(G) and FWHM(G)@244 as a function of the H content. For H contents over 20 at. %, Disp(G) increases linearly with H content, while FWHM(G)@244 shows a maximum at 25 at. % H and then decreases. The decrease of FWHM(G) and the increase of Disp(G) is different from the case of H-free carbon films, where FWHM(G) and Disp(G) increase together. This is an indication that structural and topological disorder evolve differently in highly hydrogenated samples. In fact, PLCH (~40 at. % H) and ta-C:H films both have a relatively high Disp(G) (~0.3 cm^{-1}/nm), but the FWHM(G)@244 of ta-C:H is larger than that of PLCH with H=40 at. % (165 and 120 cm^{-1}, respectively). On the other hand, FWHM(G)@244 is similar for GLCH and PLCH, but Disp(G) is smaller for GLCH (~0.10 cm^{-1}/nm). Thus, *both* Disp(G) and FWHM(G) values are essential to derive the carbon bonding in a-C:H.

Figure 13 plots Pos(G)@244 as a function of H content. Pos(G)@244 increases with H content, moving up to

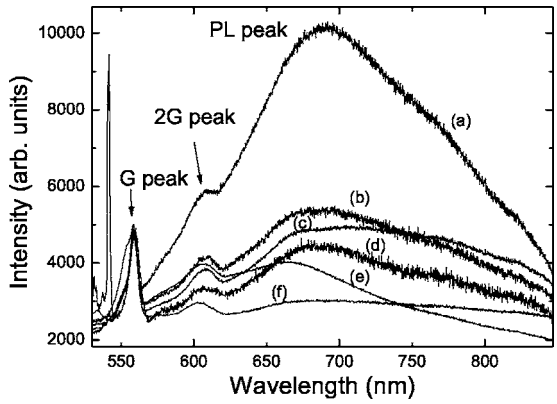

FIG. 8. Room temperature PL spectra for different amorphous carbons: (a) PLCH with 35 at. % H, (b) DLCH with 30 at. % H, (c) DLCH with 25 at. % H, (d) ta-C, (e) ta-C:H, and (f) sputtered a-C.

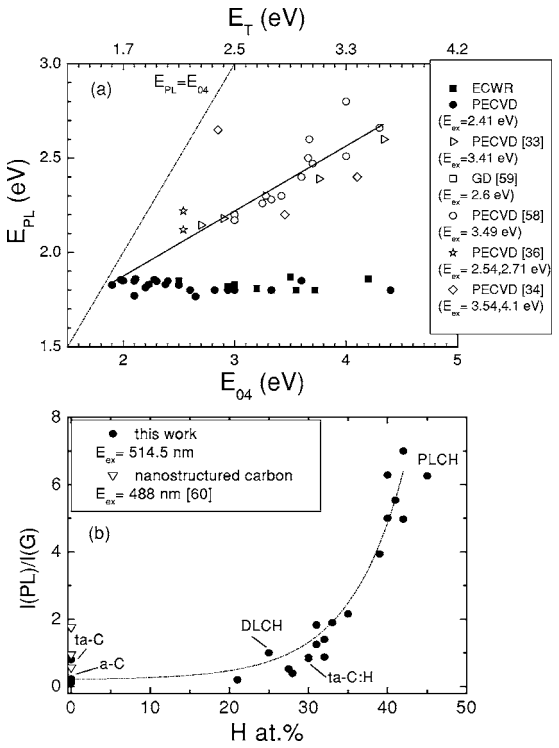

FIG. 9. (a) Variation of the PL energy with E_{04}. (b) $I(\mathrm{PL})/I(G)$ as a function of H content. Note that a-C, DLCH with H <25 at. % and ta-C:H show a very weak PL, compared with PLCH. The lines are guides to the eye.

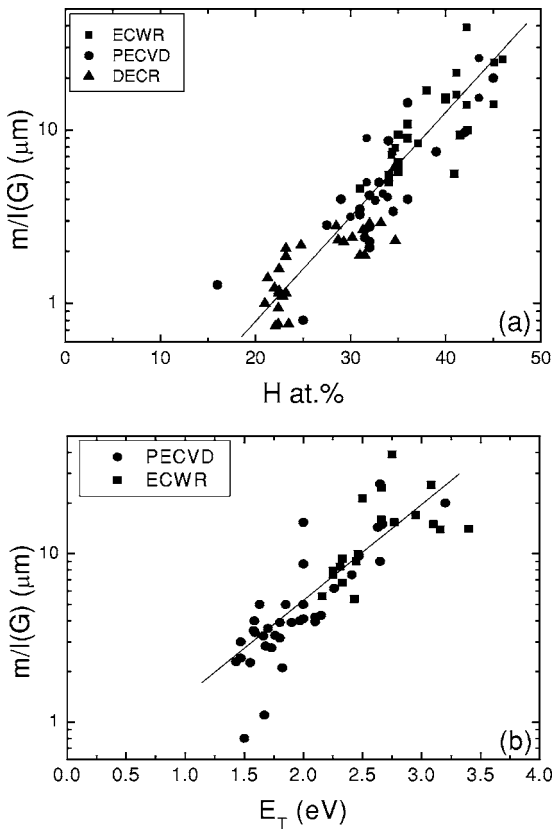

FIG. 10. $m/I(G)$ as a function of (a) H content and (b) Tauc gap. The linear fits to the data are shown.

$\sim 1625\ \mathrm{cm}^{-1}$ for PLCH films. However, for ta-C:H, Pos(G)@244 is slightly higher ($\sim 1615\ \mathrm{cm}^{-1}$) than the corresponding DLCH samples with the same H content. This is due to the higher fraction of C—C sp^3 bonds in ta-C:H.[18]

UV Raman also allows the direct detection of C—H bonds. This is shown in Fig. 14, where a broad peak due to CH_x stretching is seen at 2920–2970 cm^{-1}. The other band at $\sim 3220\ \mathrm{cm}^{-1}$ is the second order G peak, as demonstrated by H-D isotopic substitution experiments.[18] ta-C:H has a very broad and small second-order G peak compared to PLCH. The CH_x band is quite broad and it is difficult to properly deconvolute the separate contributions of sp^3 CH_x ($x=2,3$) and CH sp^2 aromatic and olefinic vibrations.[52] Infrared spectroscopy is certainly preferable for a quantitative analysis of CH_x stretching modes.[54,55] On the other hand, Raman measurements can be performed on any substrate or shape, such as metal cutting tools, which are not suitable for IR measurements. It is thus useful to analyze the CH-related UV Raman features. If the broad CH_x peak is fitted with a single Gaussian, its average position shifts from 2920 cm^{-1} for PLCH and GLCH to 2960 cm^{-1} in ta-C:H. This shift can be interpreted as a lower CH sp^3 content or a higher sp^2 olefinic or aromatic contribution in ta-C:H, compared to PLCH or GLCH.[53–55]

V. DISCUSSION

We now extend the three stage model for the Raman spectra of amorphous carbons to fully describe the structural evolution of a-C:H films for increasing H content.

As in our previous study of carbon nitrides,[26] the easiest way to visualize the modification due to heteroatoms is to compare the properties to the corresponding pure carbon film. Since hydrogen can only bond at a terminal site, its effects are in principle quite different from nitrogen.

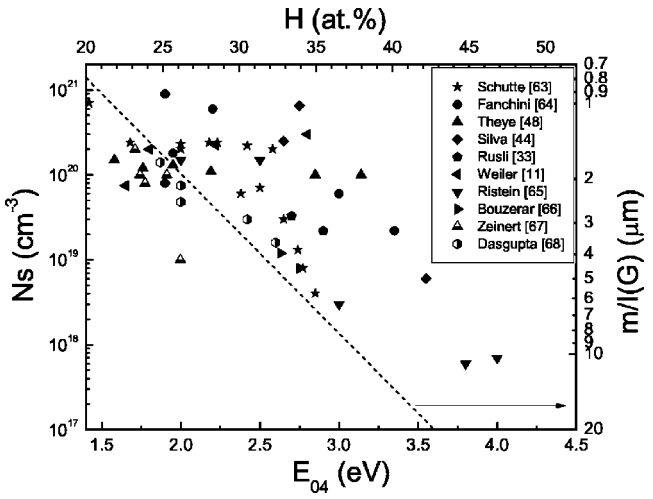

FIG. 11. Defect density and PL efficiency $[m/I(G)]$ as a function of gap (bottom X axis) and H content (top X axis). For clarity, instead of plotting all the experimental data points as in Fig. 10, we only plotted the linear fit (dotted line) representing $m/I(G)$ as a function of gap or H content.

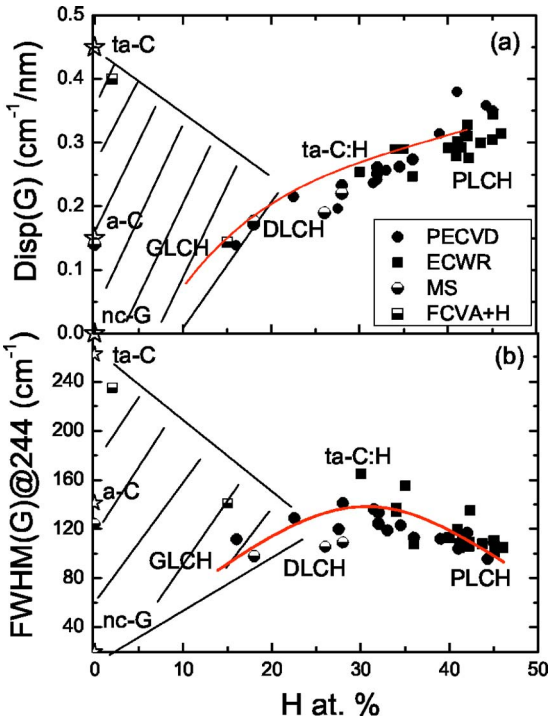

FIG. 12. (Color online) (a) Disp(G) and (b) FWHM(G)@244 as a function of H content. The ideal trajectories of the Raman parameters with H incorporation from nc-G are marked by a line. The shaded regions represent the nonuniqueness at low H contents.

A. 0 < H < 20 at. %

In this region the H content is too low to decouple the evolution of structural and topological disorder. The Raman parameters can be interpreted as in H-free films.

(1) If H is introduced in an otherwise nanocrystalline graphitic carbon, it breaks bonds and increases the bond angle and bond length disorder. This is reflected in an increase of both Disp(G) and FWHM(G)@244, Figs. 12(a) and 12(b). Thus, the size of the sp^2 clusters decreases so that $I(D)/I(G)$ decreases as in Fig. 5(b). GLCH samples can be seen as the result of H incorporation in nc-G. The ideal trajectories, describing the modification of the Raman parameters with a H incorporation in an otherwise nc-G, are indicated by a line in Figs. 5–7 and 12.

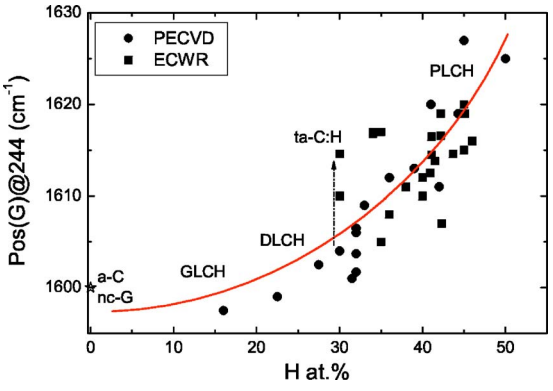

FIG. 13. (Color online) Pos(G)@244 as a function of H content. The line is a guide to the eye.

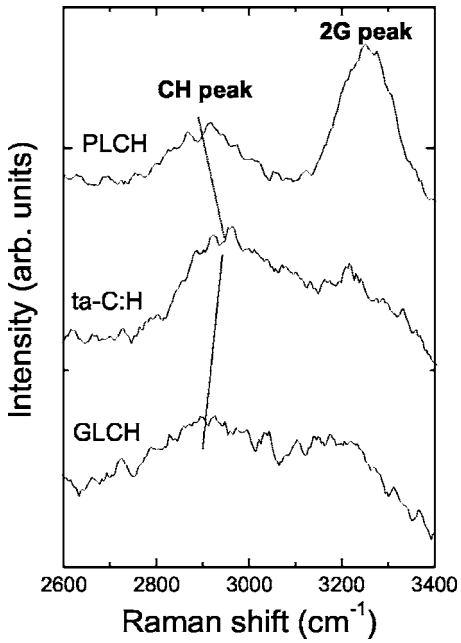

FIG. 14. UV Raman spectra showing the CH peak and second order of the G peak for template PLCH, ta-C:H, and GLCH films.

(2) If H is introduced in ta-C, this increases the order and clustering in the structure.[13] Thus, Disp(G) and FWHM(G) decrease, while $I(D)/I(G)$ increases [Figs. 5(b), 12(a), and 12(b)].

(3) If H is introduced in a mainly sp^2 amorphous carbon, a-C, it can produce both disordering and ordering effects, and they tend to compensate.

Generally speaking, for low H contents, the nonhydrogenated sp^2 phase can easily display all the nonuniqueness effects typical of low sp^3 carbons, as indicated by the shadowed regions in Figs. 5–7 and 12.

B. H > 20 at. %

For higher H contents, however, the situation is different. Although the increase in H drastically reduces the size of ring-like sp^2 structures, it steadily reduces the density and strain in the samples. The sp^2 phase is still topologically disordered, but the structural disorder is lowered. Furthermore, as-deposited samples tend to evolve in a unique way as a function of H content, thus minimizing hysteresis.

In this region, Pos(G)@514 and $I(D)/I(G)$@514 decrease with H as in Figs. 5(a) and 5(b). Disp(G) continues to increase with H, but FWHM(G) reaches a maximum for ta-C:H and then decreases for PLCH [Figs. 12(a) and 12(b)]. Similarly, Pos(G)@514 in PLCHs decreases to ~1520 cm^{-1}, before being overshadowed by the PL background, Figs. 4 and 5(a). In contrast, in ta-C Pos(G)@514 reaches ~1570 cm^{-1}, Fig. 5(a). PLCHs also show an higher Disp(G) than ta-C:H, Fig. 12(a). Within hydrogenated carbon films, ta-C:H shows the highest FWHM(G), and ta-C has the highest FWHM(G) of all carbons, for any given excitation energy.

As expected, $I(D)/I(G)$ goes to zero for both PLCH and ta-C and is small for ta-C:H, Fig. 5(b), since it is a measure

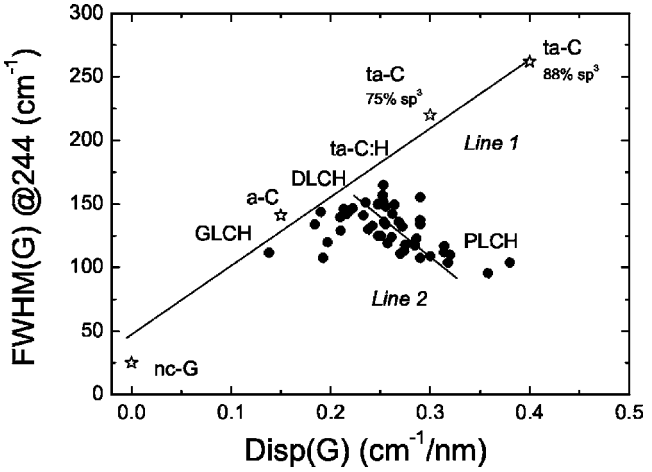

FIG. 15. Correlation between Disp(G) and FWHM(G)@244 for carbon films. The lines are guides to the eye.

of sp^2 rings and no rings are present in ta-C or PLCH.

Thus, Disp(G) and FWHM(G) do not follow the same trends as a function of H content. This differs from the behavior in H-free carbons, where an increase of Disp(G) is always accompanied by a higher FWHM(G), but just reflects the decoupling of structural disorder from topological disorder. These effects are summarized in Fig. 15, which is the key result of this paper.

For H-free carbons Disp(G) and FWHM(G) are always proportional and have the same trend as a function of the sp^3 content in Fig. 15 (Line 1). ta-C:H and GLCH also lie on Line 1. In contrast, all the samples with $H>25-30$ at. %, from DLCH to PLCH, follow the opposite trend (Line 2) in Fig. 15. Thus, in general, the same FWHM(G)@244, if lower than $\sim 170\ \mathrm{cm}^{-1}$, is associated to two different Disp(G), depending on the H content. In contrast, the same Disp(G), if over 0.2 cm^{-1}/nm, is associated with two different FWHM(G)@244 values. However, if one performs a multi-wavelength investigation and combines Disp(G) *and* FWHM(G)@244, one can uniquely characterize the carbon films.

We now relate the parameters FWMH(G) and Disp(G) to the underlying bonding properties. Since FWHM(G) is influenced by the structural disorder, we expect this to be the key parameter to uniquely measure the structural and mechanical properties, which ultimately depend on the amount of C—C sp^3 bonds for any a-C:H film. On the other hand, we expect Disp(G) to be very sensitive to the evolution of the sp^2 phase in any hydrogenated carbon film, and to be uniquely related to the optical properties and hydrogen content.

Since for low H contents Disp(G) and FWHM(G) have the same trends, and for high H contents Disp(G) uniquely evolves with H, and thus with the amount of C—H sp^3 bonds, we expect a relation between Disp(G) and the total sp^3 content in a-C:H (C—C sp^3+C—H sp^3). This is demonstrated in Fig. 16. Note that ta-C:H and ta-C lie outside the a-C:H line in Fig. 16.

However, since density and Young's modulus mainly depend on the C—C sp^3 content, in hydrogenated carbons they cannot be measured by Disp(G), but by FWHM(G), Figs. 17(a) and 17(b).

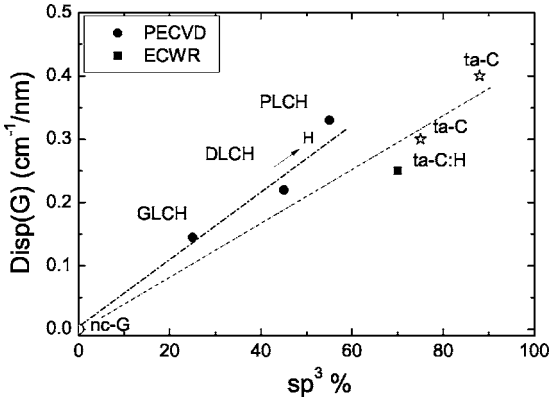

FIG. 16. Correlation between Disp(G) and total C—C+C—H sp^3 content in hydrogenated carbon films. Sp^3 data from Refs. 4 and 17.

From a linear fit of the data in Figs. 17(a) and 17(b), we get the following simple relations for $H>20$ at. %:

$$\rho\ [\mathrm{g/cm^3}] = 0.257 + 0.011W\ [\mathrm{cm^{-1}}], \tag{4}$$

$$E\ [\mathrm{GPa}] = -511 + 4.66W\ [\mathrm{cm^{-1}}], \tag{5}$$

where W=FWHM(G)@244.

Figure 18 shows the variation of mass density with sp^3 fraction for the different carbon films.[8] For H-free carbons, the density increases monotonically and linearly with sp^3 fraction. A similar behavior is found for GLCH and DLCH up to a certain density. Then the ta-C:Hs continue to increase monotonically, whereas the PLCHs turn over and the density decreases for higher sp^3 values. The similar trends in Figs.

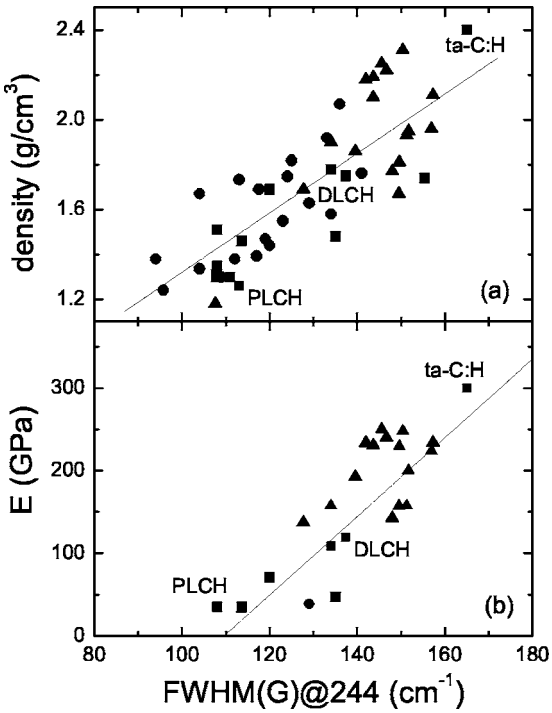

FIG. 17. (a) Density and (b) Young's modulus as a function of FWHM(G)@244. The linear fits are shown.

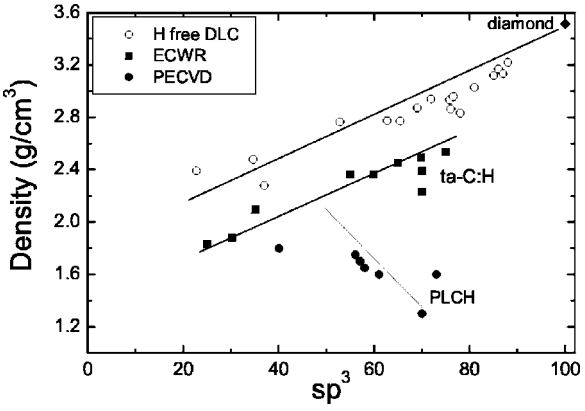

FIG. 18. Density as a function of the sp^3 content for H free and hydrogenated amorphous carbons (Ref. 8).

15 and 18 again confirm that FWHM(G) and Disp(G) are related with density and total sp^3 content, respectively.

Disp(G), being a measure of topological disorder, is also a good measure of the band gap in hydrogenated carbons, as shown in Fig. 19. Given also that the Urbach energy E_U varies roughly linearly with gap, we expect Disp(G) and E_U to be linearly related. Thus, Fig. 15 is also the equivalent of the E_U versus optical gap relation found for hydrogenated amorphous carbons.[1,30] E_U is defined as the inverse of the slope of $\ln[\alpha(E)]$ at the E_{03} energy, where $\alpha(E)$ is the optical absorption and E_{03} is the photon energy at which the absorption coefficient reaches 10^3 cm^{-1}.[1,30,69] In fully sp^3 semiconductors, E_U increases with the amount of disorder and the spin density,[69] but for PLCH E_U increases for decreasing spin density.[30] From Fig. 20, we see that E_U and Disp(G) have the same trends, thus the same physical meaning. Figure 20 demonstrates that E_U is a measure of structural disorder, as in a-Si:H, *only* in low or no hydrogen content samples. On the other hand, for high H content samples, E_U is a measure of topological disorder, as suggested in Ref. 30.

It is then easy to understand why by plotting density versus gap we get Fig. 21. As expected, we find two different

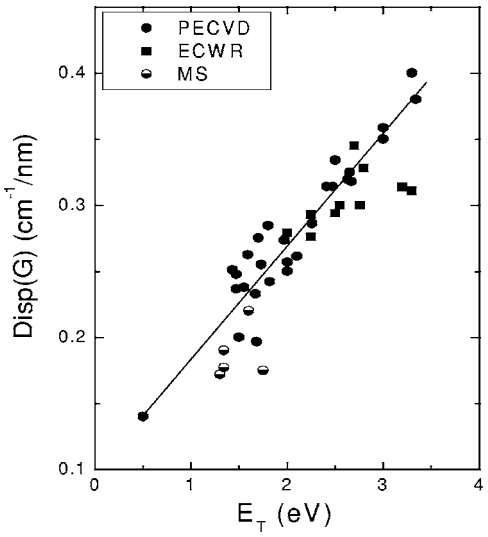

FIG. 19. Disp(G) as a function of Tauc gap. The linear fit is shown.

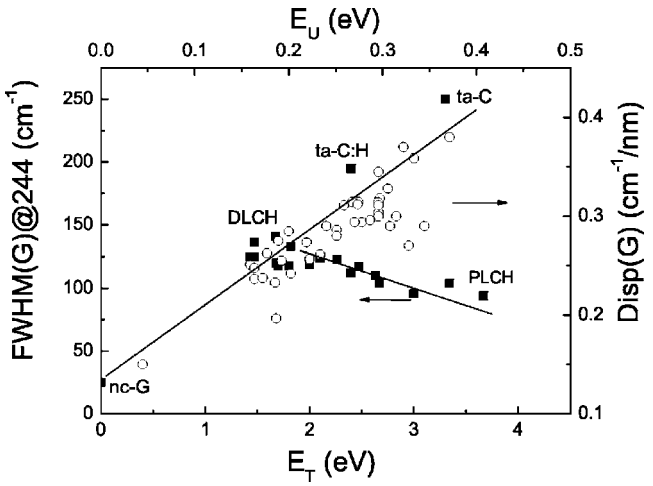

FIG. 20. Correlation between Raman parameters, Urbach energy, and Tauc gap. The lines are guides to the eye.

relations between optical gap and density. Note that DLCHs represent a junction between the two lines, as it was in Fig. 15.

If we restrict ourselves to a-C:Hs with high hydrogen content (i.e., on line 2), we can get other useful relations, valid *only in this regime*.

Figure 22 plots the square of the refractive index measured as a function of the density. By fitting Fig. 22 we find

$$n^2 = -1 + 3.38 \cdot \rho \ [\mathrm{g/cm^3}]. \tag{6}$$

By combining Eqs. (4)–(6) we also get

$$n^2 = -0.13 + 3.7 \times 10^{-2} W \ [\mathrm{cm^{-1}}]. \tag{7}$$

From Fig. 21 we get the relation between optical gap and density

$$E_T \ (\mathrm{eV}) = 4.6 - 1.6\rho \ [\mathrm{g/cm^3}]. \tag{8}$$

By combining Eqs. (5)–(8) we get

$$E_T \ (\mathrm{eV}) = 4.2 - 1.6 \times 10^{-2} \ W \ [\mathrm{cm^{-1}}]. \tag{9}$$

It is interesting to note that the linear relation between n^2 and the density of Fig. 22 confirms that in hydrogenated amor-

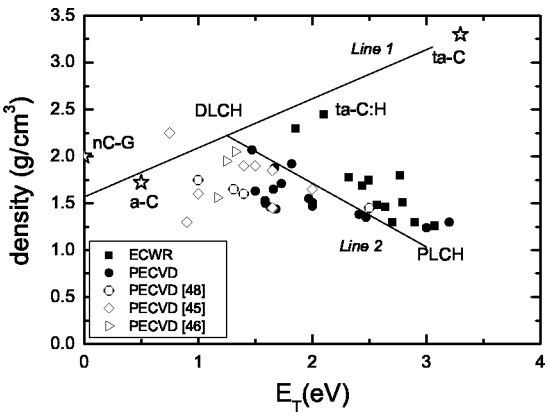

FIG. 21. Density plotted as a function of the Tauc gap. The lines are guides to the eye.

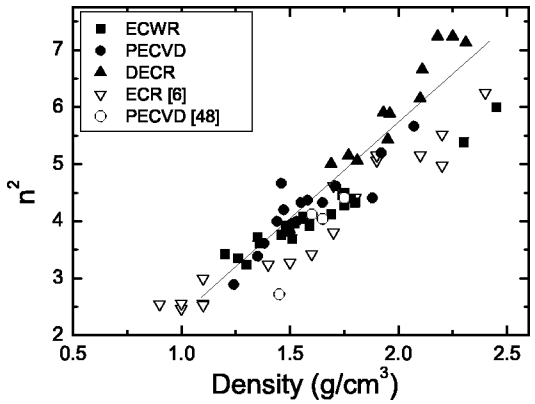

FIG. 22. Square of the refractive measured at 633 nm (with some data at 600 nm) as a function of density.

phous carbons the product $E_G m^* \sim$ constant, where m^* is the interband effective electron mass and E_G is the Penn gap, i.e., the average bonding antibonding splitting.[8] A similar linear trend is reported in Ref. 70.

C. H > 20 at. % and sp^2 phase clustered in rings

This case corresponds to PLCH containing sp^2 rings or to a highly hydrogenated GLCH. We call this class of materials GLCHH. This seems to be a very peculiar case, but has been found in literature.[71,72] GLCHH is typically produced by PECVD from a mixture of CH_4 and H_2 and very high bias voltage.[71,72] Typical Raman spectra of GLCHH measured at 244 and 514 nm are plotted in Fig. 23 and compared with GLCH and PLCH samples. Figure 24 upgrades Fig. 12 to include GLCHHs. The Raman parameters are very close to GLCH, as expected from the more ring-like sp^2 configuration, which reduces Disp(G) with respect to PLCHs. However, the visible Raman spectrum shows a higher PL background than standard GLCH. Typically $m/I(G)$ for GLCHH is ~ 5 μm. Indeed, the H content is 30–40 at. %,[73] Figs. 24(a) and 24(b). The density of these samples can be as low as 1.3 g/cm^3, below the density of typical GLCH ($\sim$1.6 g/cm^3). Thus, in order to identify GLCHH films we need to combine the analysis of Disp(G) and FWHM(G) with the PL background.

GLCHH films have interesting technological applications. Even though the mechanical properties of these samples can be very poor, they can show excellent friction behavior in vacuum or dry nitrogen.[71,72,74] Thus, H content *per se* is not the only parameter controlling the friction in *a*-C:Hs, in agreement with Refs. 75–78. Indeed, PLCH films do not show a friction coefficient as low as GLCHH with the same H content.[75–78] It is the optimal combination of high H content *and* sp^2 configuration, which gives the best frictional properties. This will be discussed in detail elsewhere.[79]

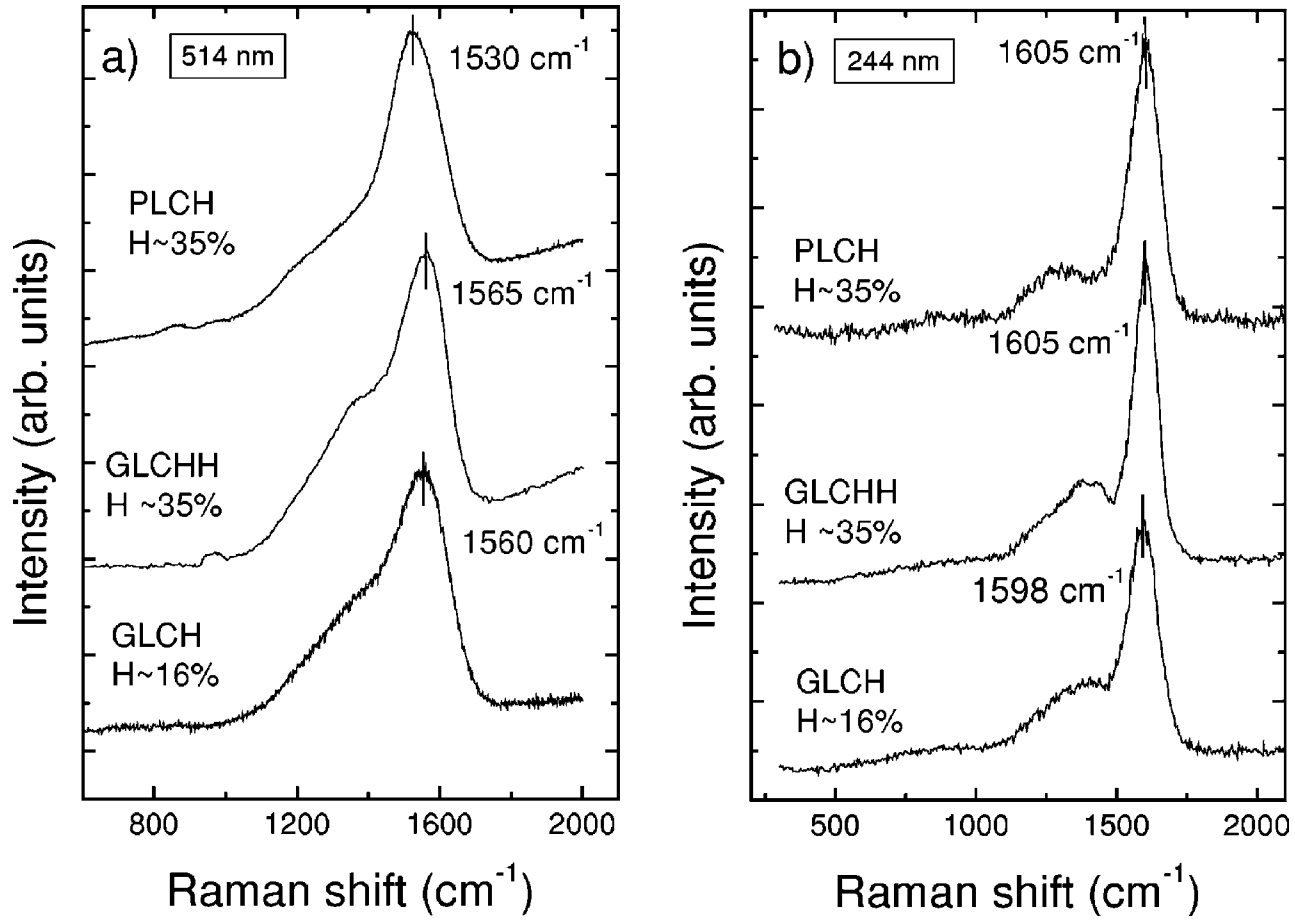

FIG. 23. Raman spectra of PLCH, GLCHH, and GLCH films at (a) 514.5 and (b) 244 nm.

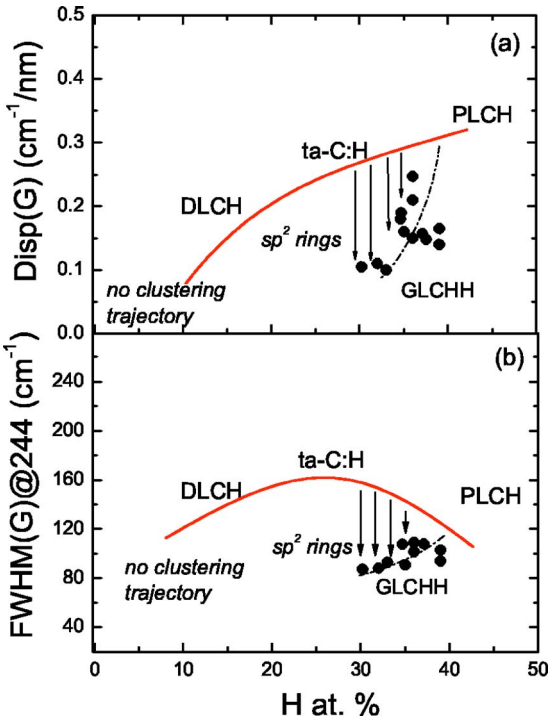

FIG. 24. (Color online) (a) Disp(G) and (b) FWHM(G)@244 as a function of the H content for amorphous carbons, including GLCHH.

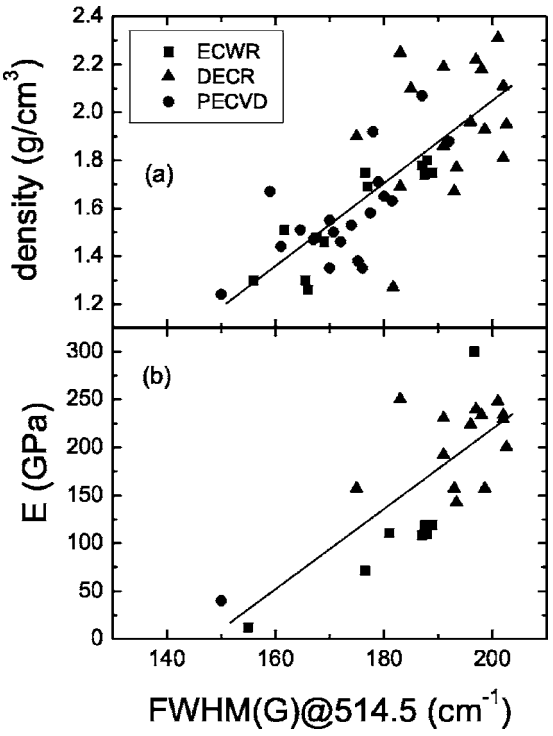

FIG. 25. (a) Density and (b) Young's modulus as a function of FWHM@514.5. The lines are guides to the eye.

Disp(G) decreases for increasing sp^2 clustering[18] and is zero if the sp^2 phase is ordered in rings. Thus, for GLCHH this parameter cannot be related to the H content, as shown in Fig. 24(a). Disp(G) is in any case related the optical gap, since the optical gap is uniquely defined by the sp^2 phase clustering. Thus, for GLCHH, Eq. (2) fails. However, the PL background can still be used to estimate the H content.

VI. MULTI-WAVELENGTH OR SINGLE WAVELENGTH RAMAN MEASUREMENTS?

From Secs. IV and V it is clear that a multi-wavelength analysis is always recommended with a-C:H, as for any other carbon. This can be restricted to only two wavelengths, such as 244 and 514 nm.

However, single wavelength measurements of a-C:H can give reliable qualitative information, especially when the H content is over 20 at. %. Even if, so far, we mostly discussed FWHM(G)@244, we get similar trends by using FWHM(G)@514, or indeed any other excitation wavelength, see Figs. 25(a) and 25(b). However, for 514 nm excitation, due to the PL background, the fit is less accurate and the data spread is larger than at 244 nm. Furthermore, 244 nm excitation is necessary in order to get a FWHM(G) for high H content PLCHs, which do not show almost any measurable Raman peaks for 514 nm. On the other hand, a featureless visible Raman spectrum with no clear Raman peaks can be taken as an empirical signature of PLCH with low density ($\leqslant 1.2$ g/cm^3) and low Young's modulus ($\leqslant 20$ GPa).

In a single wavelength analysis, the crucial parameters are (1) FWHM(G), still related with structural disorder and the C—C sp^3 content, (2) $I(D)/I(G)$, correlated to the amount of ring-like sp^2 clusters, and (3) the PL background.

Figure 26 plots FWHM(G)@514 as a function of $A(D)/A(G)$@514. Note that in this particular case we use $A(D)/A(G)$ instead of $I(D)/I(G)$ in order to compare with literature data, which usually report only $A(D)/A(G)$. This figure is again analog to Fig. 15, if one considers the opposite trends of Disp(G) and $A(D)/A(G)$. Thus, the density and Young's modulus can be derived from FWHM(G)@514 and the optical gap from $A(D)/A(G)$@514. Further information

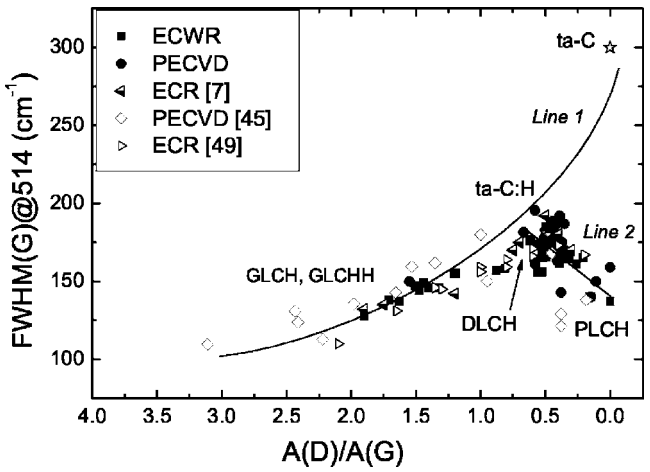

FIG. 26. FWHM(G)@514.5 as a function of $A(D)/A(G)$@514. The lines are guides to the eye.

can be derived by measuring the refractive index and using Fig. 22. The gap can then be cross checked with Fig. 21.

VII. CONCLUSIONS

We have presented a comprehensive analysis of a variety of *a*-C:H films grown by different deposition techniques and conditions. We extended the three-stage model for the Raman spectra of carbon films to the case of hydrogenated amorphous carbons. The most important parameters to interpret the *a*-C:H Raman spectra are the *G* peak dispersion and the FWHM(*G*) measured at 244 nm. The Raman spectra of *a*-C:Hs show two fundamentally different behaviors. In one case the *G* peak width increases as the *G* peak dispersion increases. In the other case, the *G* peak width decreases with increasing *G* dispersion. In the first case the correlation of the Raman parameters to the structural and mechanical properties of the films is the same as for hydrogen-free carbon films. In the second case, typical of polymeric hydrogenated amorphous carbons, the *G* peak width is correlated to the structural properties, while the *G* peak dispersion is the best parameter to probe the optical properties and the hydrogen content. The unified diagram of *G* width and *G* dispersion for the various carbons maps onto the variation of density against sp^3 fraction. This allows us to identify the *G* width as a measure of structural disorder (bond angle and bond length distortions) and, thus, of density and Young's modulus. The *G* dispersion is found to be a measure of topological disorder (range of cluster/chains sizes) and is proportional to the total (C—C+C—H) sp^3 fraction, gap, Urbach energy and H content.

The PL background measured for visible excitation can be used to estimate the H content, if H > 20 at. %. If UV Raman is not available, visible Raman spectra can be used for a qualitative characterization, but high caution must be taken in doing so. Particular deposition processes or substrate annealing can induce sp^2 clustering in *a*-C:H, even with relatively high H content. In this case, the relation between sp^3 content and sp^2 configuration fails. In general, a multiwavelength analysis is always advisable in order to avoid confusion.

ACKNOWLEDGMENTS

The authors would like to thank D. Batchelder and I. R. R. Mendieta of the University of Leeds and D. Wolverson of the University of Bath for UV Raman facilities; F. Piazza, S. E. Rodil, B. Kleinsorge, B. Popescu, A. Champi, A. Erdermir, and J. Fontaine, for some of the samples and useful discussions. The authors acknowledge D. Schneider for Young's modulus measurements and D. Grambole for hydrogen content and density measurements. A.C.F acknowledges funding from The Royal Society. This work has been supported by the European Community (FAMOUS; Project No. IST-2000-28661).

*Electronic address: acf26@eng.cam.ac.uk

[1] J. Robertson, Mater. Sci. Eng., R. **R37**, 129 (2002).
[2] P. Koidl, C. Wagner, B. Discheler, J. Wagner, and M. Ramsteiner, Mater. Sci. Forum **52**, 41 (1990).
[3] W. Jacob and W. Moller, Appl. Phys. Lett. **63**, 1771 (1993).
[4] M. A. Tamor, W. C. Vassell, and K. R. Carduner, Appl. Phys. Lett. **58**, 592 (1991).
[5] S. F. Yoon, K. H. Tan, Rusli, and J. Ahn, J. Appl. Phys. **91**, 1634 (2002).
[6] T. Schwarz-Selinger, A. von Keudell, and W. Jacob, J. Appl. Phys. **86**, 3988 (1999).
[7] O. Durand-Drouhin, M. Lejeune, and M. Benlahsen, J. Appl. Phys. **91**, 867 (2002).
[8] A. C. Ferrari, A. Libassi, B. K. Tanner, V. Stolojan, J. Yuan, L. M. Brown, S. E. Rodil, B. Kleinsorge, and J. Robertson, Phys. Rev. B **62**, 11089 (2000).
[9] N. A. Morrison, S. E. Rodil, A. C. Ferrari, J. Robertson, and W. I. Milne, Thin Solid Films **337**, 71 (1999).
[10] M. Weiler, K. Lang, E. Li, and J. Robertson, Appl. Phys. Lett. **72**, 1314 (1998).
[11] M. Weiler, S. Sattel, T. Giessen, K. Jung, H. Ehrhardt, V. S. Veerasamy, and J. Robertson, Phys. Rev. B **53**, 1594 (1996).
[12] M. Weiler, S. Sattel, K. Jung, H. Ehrhardt, V. S. Veerasamy, and J. Robertson, Appl. Phys. Lett. **64**, 2797 (1994).
[13] B. Kleinsorge, S. E. Rodil, G. Adamopoulos, J. Robertson, D. Grambole, and W. Fukarek, Diamond Relat. Mater. **10**, 965 (2001).
[14] B. Meyerson and F. Smith, J. Non-Cryst. Solids **35–36**, 435 (1980).
[15] B. Popescu, A. Tagliaferro, F. De Zan, and E. A. Davis, J. Non-Cryst. Solids **266–269**, 803 (2000).
[16] A. C. Ferrari and J. Robertson, Philos. Trans. R. Soc. London, Ser. A **362**, 2267 (2004).
[17] A. C. Ferrari and J. Robertson, Phys. Rev. B **61**, 14095 (2000).
[18] A. C. Ferrari and J. Robertson, Phys. Rev. B **64**, 075414 (2001).
[19] S. Piscanec, F. Mauri, A. C. Ferrari, M. Lazzeri, and J. Robertson, Diamond Relat. Mater. **14**, 1078 (2005).
[20] K. W. R. Gilkes, S. Prawer, K. W. Nugent, J. Robertson, H. S. Sands, Y. Lifshitz, and X. Shi, J. Appl. Phys. **87**, 7283 (2000).
[21] V. I. Merkulov, J. S. Lannin, C. H. Munro, S. A. Asher, V. S. Veerasamy, and W. I. Milne, Phys. Rev. Lett. **78**, 4869 (1997).
[22] F. Tuinstra and J. L. Koenig, J. Chem. Phys. **53**, 1126 (1970).
[23] C. Castiglioni, E. Di Donato, M. Tommasini, F. Negri, and G. Zerbi, Synth. Met. **139**, 885 (2003).
[24] S. Piscanec, M. Lazzeri, F. Mauri, A. C. Ferrari, and J. Robertson, Phys. Rev. Lett. **93**, 185503 (2004).
[25] C. Mapelli, C. Castiglioni, G. Zerbi, and K. Mullen, Phys. Rev. B **60**, 12710 (2000).
[26] A. C. Ferrari, S. E. Rodil, and J. Robertson, Phys. Rev. B **67**, 155306 (2003).
[27] A. C. Ferrari and J. Robertson, Phys. Rev. B **63**, 121405(R) (2001).
[28] C. Casiraghi, A. C. Ferrari, J. Robertson, R. Ohr, M. v. Gradowski, and D. Schneider, Diamond Relat. Mater. **13**, 1480

(2004).
[29] M. v. Gradowski, A. C. Ferrari, R. Ohr, B. Jacoby, H. Hilgers, H.-H. Schneider, and H. Adrian, Surf. Coat. Technol. **174–175**, 246 (2003).
[30] G. Fanchini and A. Tagliaferro, Appl. Phys. Lett. **85**, 730 (2004).
[31] A. C. Ferrari, B. Kleinsorge, N. A. Morrison, A. Hart, V. Stolojan, and J. Robertson, J. Appl. Phys. **85**, 7191 (1999).
[32] J. Robertson, Phys. Rev. B **53**, 16302 (1996).
[33] Rusli, J. Robertson, and G. A. J. Amaratunga, J. Appl. Phys. **80**, 2998 (1996).
[34] T. Heitz, C. Godet, J. E. Bouree, B. Drevillon, and J. P. Conde, Phys. Rev. B **60**, 6045 (1999).
[35] B. Marchon, J. Gui, K. Grannen, G. C. Rauch, J. W. Ager, S. R. P. Silva, and J. Robertson, IEEE Trans. Magn. **33**, 3148 (1997).
[36] S. Xu, M. Humdhausen, J. Ristein, B. Yan, and L. Ley, J. Non-Cryst. Solids **164**, 1127 (1993).
[37] Q. Zhang, S. F. Yoon, Rusli, J. Ahn, H. Yang, and D. Bahr, J. Appl. Phys. **84**, 5538 (1998).
[38] S. F. Yoon, K. H. Tan, Rusli, J. Ahn, and Q. F. Huang, J. Appl. Phys. **89**, 4830 (2001).
[39] F. Piazza, D. Grambole, D. Schneider, C. Casiraghi, A. C. Ferrari, and J. Robertson, Diamond Relat. Mater. **14**, 994 (2005).
[40] A. Golanski, F. Piazza, J. Werckmann, G. Relihan, and S. Schulze, J. Appl. Phys. **92**, 3662 (2002).
[41] F. Piazza, Y. Arnal, D. Grambole, F. Herrmann, M. Kildemo, A. Lacoste, G. Relihan, and A. Golanski, Thin Solid Films **383**, 196 (2001).
[42] F. Piazza (unpublished).
[43] B. Popescu, C. Verney, E. A. Davis, V. Paret, and A. Brunet-Bruneau, J. Non-Cryst. Solids **266–269**, 778 (2000).
[44] S. R. P. Silva, J. Robertson, Rusli, and G. A. J. Amaratunga, Philos. Mag. B **74**, 369 (1996).
[45] M. A. Tamor and W. C. Vassell, J. Appl. Phys. **76**, 3823 (1994).
[46] E. Tomasella, C. Meunier, and S. Mikhailov, Surf. Coat. Technol. **141**, 286 (2001).
[47] R. Bouzerar, C. Amory, A. Zeinert, M. Benlahsen, B. Racine, O. Durand-Drouhin, and M. Clin, J. Non-Cryst. Solids **281**, 171 (2001).
[48] M. L. Theye, V. Paret, and A. Sadki, Diamond Relat. Mater. **10**, 182 (2001).
[49] Rusli, S. F. Yoon, H. Yang, J. Ahn, Q. Zhang, Y. S. Wu, and W. L. New, J. Appl. Phys. **84**, 5277 (1998).
[50] C. Marechal, A. Zeinert, K. Zellama, E. Lacaze, M. Zarrabian, and G. Turban, Solid State Commun. **109**, 23 (1999).
[51] D. Schneider, T. Schwarz, H.-J. Scheibe, and M. Panzner, Thin Solid Films **295**, 107 (1997).
[52] A. C. Ferrari, J. Robertson, M. G. Beghi, C. E. Bottani, R. Ferulano, and R. Pastorelli, Appl. Phys. Lett. **75**, 1893 (1999).
[53] F. R. Dollish, W. G. Fateley, and F. F. Bentley, *Characteristic Raman Frequencies of Organic Molecule* (Wiley, New York, 1974).
[54] B. Dischler, A. Bubenzer, and P. Koidl, Solid State Commun. **48**, 105 (1983).
[55] J. Ristein, R. T. Stief, L. Ley, and W. Beyer, J. Appl. Phys. **84**, 3836 (1998).
[56] G. Fanchini, P. Mandracci, A. Tagliaferro, S. E. Rodil, A. Vomiero, and G. Della Mea, Diamond Relat. Mater. **14**, 928 (2005).
[57] S. Sattel, J. Robertson, and H. Ehrhardt, J. Appl. Phys. **82**, 4566 (1997).
[58] M. Yoshimi, M. Shimizu, K. Hattori, H. Okamoto, and Y. Hamakawa, Optoelectron., Devices Technol. **7**, 69 (1992).
[59] J. Wagner and P. Lautenschlager, J. Appl. Phys. **59**, 2044 (1986).
[60] S. J. Henley, J. D. Carey, and S. R. P. Silva, Appl. Phys. Lett. **85**, 6236 (2004).
[61] S. E. Rodil, S. Muhl, S. Maca, and A. C. Ferrari, Thin Solid Films **433**, 119 (2003).
[62] G. Fanchini, S. C. Ray, and A. Tagliaferro, Diamond Relat. Mater. **12**, 1084 (2003).
[63] S. Schutte, S. Will, H. Mell, and W. Fuhs, Diamond Relat. Mater. **2**, 1360 (1993).
[64] G. Fanchini, A. Tagliaferro, B. Popescu, and E. A. Davis, J. Non-Cryst. Solids **299–302**, 846 (2002).
[65] J. Ristein, J. Schafer, and L. Ley, Diamond Relat. Mater. **4**, 508 (1995).
[66] R. Bouzerar, A. Zeinert, and H.-J. von Bardeleben, Diamond Relat. Mater. **14**, 1108 (2005).
[67] A. Zeinert, H.-J. von Bardeleben, and R. Bouzerar, Diamond Relat. Mater. **9**, 728 (2000).
[68] D. Dasgupta, F. Demichelis, C. F. Pirri, and A. Tagliaferro, Phys. Rev. B **43**, 2131 (1991).
[69] R. A. Street, *Hydrogenated Amorphous Silicon* (Cambridge University Press, New York, 1991).
[70] P. Patsalas, S. Logothetidis, and P. C. Kelires, Diamond Relat. Mater. **14**, 1241 (2005).
[71] A. Erdemir, O. L. Eryilmaz, I. B. Nilufer, and G. R. Fenske, Diamond Relat. Mater. **9**, 632 (2000).
[72] A. Erdemir, O. L. Eryilmaz, and G. R. Fenske, J. Vac. Sci. Technol. A **18**, 1987 (2000).
[73] J. A. Johnson, J. B. Woodford, X. Chen, J. Andersson, A. Erdemir, and G. R. Fenske, J. Appl. Phys. **95**, 7765 (2004).
[74] A. Erdemir, O. L. Eryilmaz, I. B. Nilufer, and G. R. Fenske, Surf. Coat. Technol. **133–134**, 448 (2000).
[75] J. Fontaine, J. L. Loubet, T. Le Mogne, and A. Grill, Tribol. Lett. **17**, 709 (2004).
[76] J. Fontaine, T. Le Mogne, J. L. Loubet, and M. Belin, Thin Solid Films **482**, 99 (2005).
[77] A. Erdemir, Surf. Coat. Technol. **146–147**, 292 (2001).
[78] A. Erdemir, Tribol. Int. **37**, 577 (2004).
[79] C. Casiraghi, A. C. Ferrari, A. Erdemir, J. Fontaine, and J. Robertson (unpublished).